ACS OMEGA

http://pubs.acs.org/journal/acsodf

Article

Scalable and Tunable Diamond Nanostructuring Process for Nanoscale NMR Applications

Martin Gierse,*,# Alastair Marshall,# M. Usman Qureshi, Jochen Scharpf, Anna J. Parker, Birgit J. M. Hausmann, Paul Walther, Ania C. Bleszynski Jayich, Fedor Jelezko, Philipp Neumann, and Ilai Schwartz

Cite This: *ACS Omega* 2022, 7, 31544−31550

Read Online

ACCESS | Metrics & More | Article Recommendations | Supporting Information

ABSTRACT: Nanostructuring of a bulk material is used to change its mechanical, optical, and electronic properties and to enable many new applications. We present a scalable fabrication technique that enables the creation of densely packed diamond nanopillars for quantum technology applications. The process yields tunable feature sizes without the employment of lithographic techniques. High-aspect-ratio pillars are created through oxygen-plasma etching of diamond with a dewetted palladium film as an etch mask. We demonstrate an iterative renewal of the palladium etch mask, by which the initial mask thickness is not the limiting factor for the etch depth. Following the process, 300−400 million densely packed 100 nm wide and 1 μm tall diamond pillars were created on a 3 × 3 mm^2 diamond sample. The fabrication technique is tailored specifically to enable applications and research involving quantum coherent defect center spins in diamond, such as nitrogen-vacancy (NV) centers, which are widely used in quantum science and engineering. To demonstrate the compatibility of our technique with quantum sensing, NV centers are created in the nanopillar sidewalls and are used to sense ^{1}H nuclei in liquid wetting the nanostructured surface. This nanostructuring process is an important element for enabling the wide-scale implementation of NV-driven magnetic resonance imaging or NV-driven NMR.

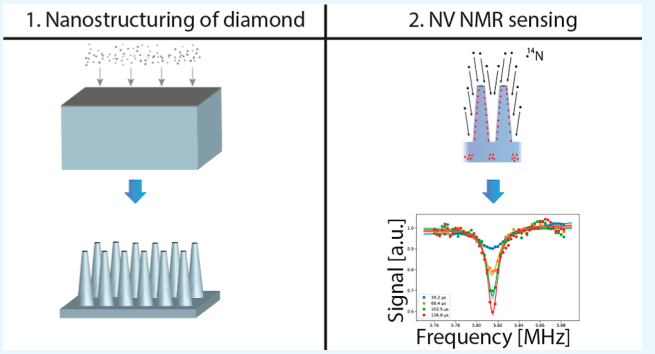

INTRODUCTION

Since the first investigation of single color centers in diamond,[1] diamond rapidly gained popularity in the field of quantum optics. One specific color center in diamond, the nitrogen-vacancy (NV) center, has been most intensively studied and shows promise for numerous applications including quantum computing,[2] quantum cryptography,[3] quantum sensing,[4−6] masers,[7] and so forth. The creation of dense ensembles of near-surface NV centers is important for many applications, including NV center-driven hyperpolarization for nuclear magnetic resonance (NMR) and magnetic resonance imaging (MRI) applications,[8] widefield imaging of condensed matter and biological systems,[9] and photonic applications.[10] In this work, the customization of diamond samples targets MRI/NMR and sensing-related applications.

The signal at thermal equilibrium in NMR or MRI applications is proportional to the nuclear spin polarization, which is determined by the magnetic field strength, temperature, and gyromagnetic ratio.[11] However, it is possible to increase nuclear spin polarization by utilizing the optically driven electron spin polarization of the ground state NV center, a polarization that can exceed 92%.[12] Theoretical investigations have hypothesized that transferring electron spin polarization from an ensemble of NV centers to nuclei external to the diamond could enhance the NMR or MRI signal up to several orders of magnitude.[13] As target molecules, metabolites are particularly interesting molecules to hyperpolarize since tracking their metabolism in real time with MRI has been shown to reveal crucial information in living organisms. An important example of this is a study by Kurhanewicz et al. who demonstrated that prostate tumors can be diagnosed utilizing the metabolism of pyruvic acid hyperpolarized via dissolution dynamic-nuclear polarization (d-DNP).[14]

To successfully exploit NV centers for hyperpolarization of external liquids, several aspects must be considered. First, the NV center ensemble and the target molecules should be close to the diamond surface to improve the interaction between the internal electron spins and the external nuclear spins. The diamond surface termination should therefore enable wetting

Received: July 6, 2022
Accepted: July 20, 2022
Published: August 24, 2022

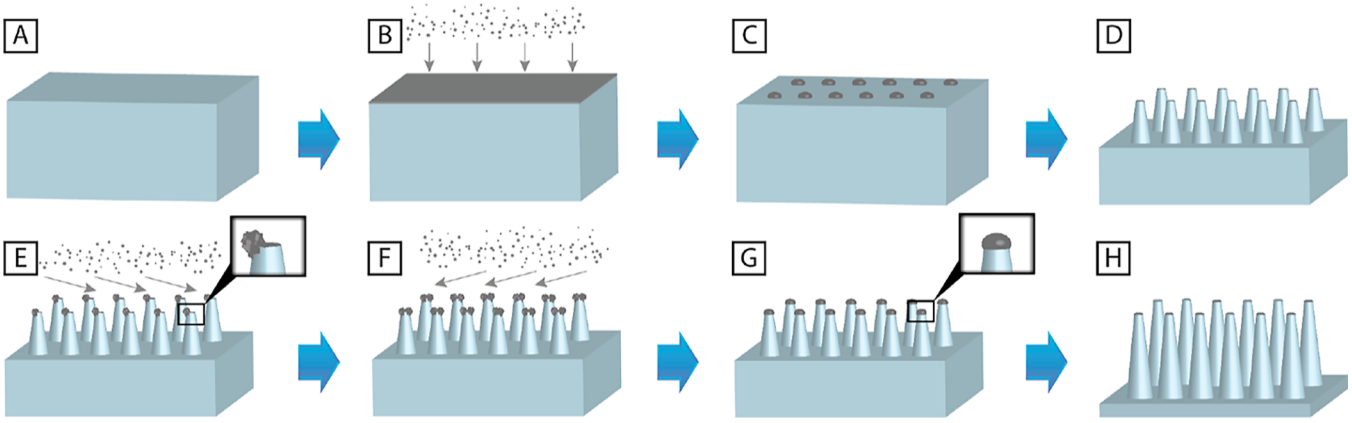

Figure 1. Schematic of the fabrication process. (A) After cleaning the diamond, (B) a thin palladium film is deposited on the diamond. (C) A thermal treatment separates the palladium film into small droplets. (D) Subsequent RIE creates the initial diamond pillars. (D) Since the palladium mask is etched away before the desired aspect ratio of the diamond pillars is reached, (E) additional palladium is deposited at an angle of 75° on the diamond. The angled deposition causes the pillars to shadow the lower parts of them, which results in an accumulation of coarse mask material at the top of the pillars. (F) This step is repeated after rotating the diamond by 180°. (G) Another thermal treatment transforms the coarse mask into a single smooth metal sphere sitting on each diamond pillar. (H) The additional mask allows for further etching and therefore for high-aspect-ratio diamond pillars.

of the liquid on the surface. A smooth diamond surface is beneficial since surface roughness is suspected to be correlated with the density of surface spins, a source of decoherence for surface NV centers.[15] Long coherence times and preferential alignment of the NV centers improve the efficiency of pulsed hyperpolarization protocols. Additionally, the volume of the hyperpolarized liquid must be macroscopic (e.g., 2 μL of neat pyruvate is required for preclinical studies in mice and around 1 mL for clinical studies),[16] meaning that it would be favorable to enhance the diamond surface area via nanostructuring. The average distance of the target molecules to the diamond surface should be short so that a significant portion of the target molecules directly interacts with the NV centers via dipole−dipole coupling, while the others are hyperpolarized via spin diffusion. This is benchmarked using the characteristic spin diffusion length of a target solution, defined as the time the nuclear spin polarization diffuses within a one spin−lattice relaxation (T_1) period. Given these considerations, we understand that the aspect ratio of the nanofeatures should be as large as possible, while the feature pitch should be less than or match the nuclear spin diffusion length of the targeted molecules. The range of spin diffusion lengths targeted in this study is estimated to be 100−300 nm for partially deuterated glasses with $[^1H]$ = 1 M with T_1 ranging from 30 to 300 s (1 T, −196 °C).[17]

In addition to polarization transfer to external nuclear spins, shallow NV centers are often applied for the detection of unpolarized nuclear spins.[18] Their depth, d, of a few nm, defines a detection volume outside the diamond roughly of the size d^3. For an ensemble of NV centers at a depth of around 5 nm, this volume contains on the order of 10,000 ^{1}H spins for water. Even if the polarization of these spins is negligible, they exhibit statistical polarization with a root-mean-square (rms) value of 100 spins for the mentioned example, which is 1% of the total spin number and thus amounts to a large detectable signal. Surface enhancement by nanostructuring also enhances the detection sensitivity of the NV ensemble and could improve its application in the sensing of unpolarized nuclear spins.

High-aspect-ratio diamond nanopillars are typically created via defining an etch mask with electron beam lithography (EBL) and subsequent reactive ion etching (RIE). This approach is highly versatile, enabling the creation of arbitrary arrangements of metal mask geometries with high accuracy and reproducibility.[19,20] The disadvantage, however, is that such a method can be costly and time-intensive, where nanostructuring a 2 × 2 mm^2 sample may require an entire day. For nanoscale sensing and hyperpolarization applications, mask and pattern geometry play a secondary role, and instead, high throughput is critical. Previously, metal colloids were applied or sputtered on the diamond surface, which enables the selective etching of diamond nanowires.[10,21] While a colloid deposition is straightforward and fast, it is difficult to control pitch while preventing the colloids from aggregating, and the choices of metal available are not necessarily best for etch-mask selectivity.[22] Alternatively, in an effect called dewetting, melting-point depression can be leveraged to create nanosized metal features: when thin metal films are heated, they often rearrange to a thermodynamically more stable configuration, for example, droplets.[23,24] This rearrangement can happen at temperatures far below the melting point of the metal depending on the film thickness. Using metal particles formed by dewetting as an etch mask on the polycrystalline diamond has been demonstrated to deposit a single mask, which yields features with up to 850 nm height post etching.[22,25] In this work, we show how to tune the process for a palladium mask, where, in particular, the mask is renewed to yield features with a range of diameter and pitch, and demonstrate pillars 1 μm tall, 100 nm diameter, with a pitch of 200 nm. The added step of mask renewal plus reannealing is crucial for achieving the high aspect ratios demanded by possible applications for NV centers in diamond.

A schematic of the process is given in Figure 1A: once the palladium film is deposited on the diamond (Figure 1B), the thermal treatment separates the palladium into small metal droplets, as shown in Figure 1C. The average size and pitch of the dewetted metal droplets can be controlled via the metal film thickness and the dewetting temperature. However, since the geometry of the droplets can be approximated by spheres,

https://doi.org/10.1021/acsomega.2c04250
ACS Omega 2022, 7, 31544−31550

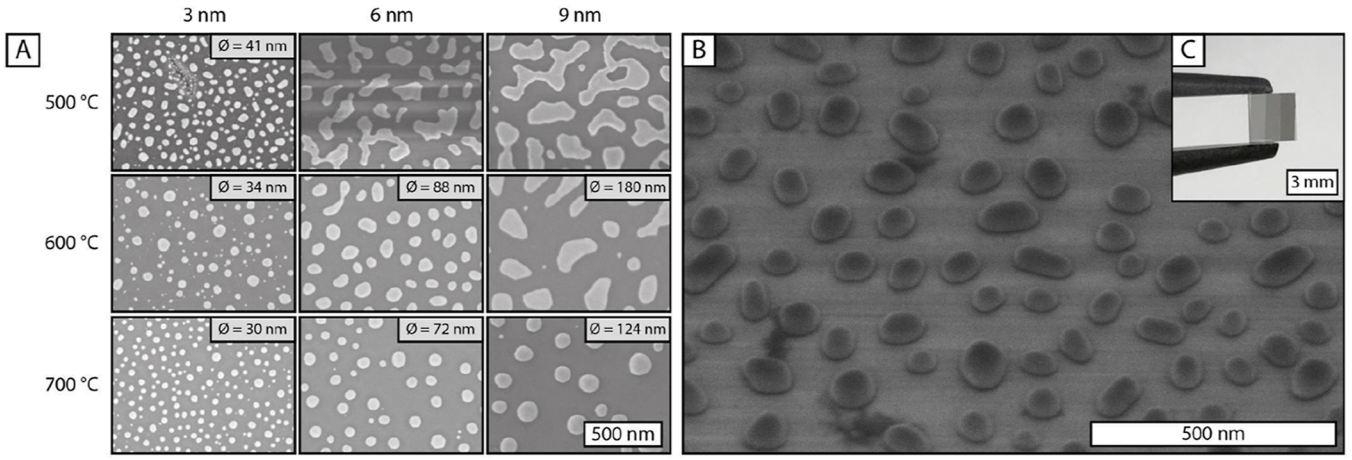

Figure 2. (A) Effect of the initial palladium film thickness and the dewetting temperature on the palladium feature size and geometry (SEM parameters: 2 kV acceleration voltage, 10 μA current, 0° tilt angle). Average diameters were calculated via ImageJ and are indicated in the insets. (B) Dewetted palladium features prior to oxygen etching. A palladium film thickness of 6 nm and a dewetting temperature of 600 °C was used. (SEM parameters: 2 kV acceleration voltage, 10 μA current, 45° tilt angle). (c) Photo of the 3 × 3 mm^2 optical grade diamond sample with three different palladium film thicknesses of 3, 6, and 9 nm.

the height of the metal features roughly matches its width. This can become a problem if high-aspect-ratio nanopillars are desired: the maximum etch time, and therefore the etch depth, is determined by the thickness of the metal mask. The palladium mask may be etched away before the desired aspect ratio of the diamond pillars is reached, as illustrated in Figure 1D. We mitigate the effects of mask erosion by developing a process for mask renewal: once the initial mask is etched away, the sample is mounted at an angle of 75° in the evaporation chamber and 20 nm palladium is then deposited from the side of the nanostructured surface. Due to shadowing, the palladium only accumulates on the upper part of the pillars, as shown in Figure 1E. Since only one side is covered by the palladium, this process step is repeated after rotating the diamond by 180°, as shown in (Figure 1F). Another run of dewetting transforms the mask material with the natural roughness of the electron beam evaporation into smooth metal spheres sitting on the tops of the nanopillars, as illustrated in Figure 1G. This technique enables additional plasma etching, resulting in 1 μm tall and 100 nm wide diamond nanopillars, with a pitch of 200 nm.

In the following sections, we also verified that pyruvic acid wets the nanostructure and that the created NVs in the pillar sidewalls can be coupled to the ^{1}H nuclei in an external liquid.

FABRICATION METHODS

To test different parameters of the nanofabrication, optical-grade diamond substrates from Element Six were used (SC Plate CVD 3.0 × 3.0 mm^2, 0.25 mm thick, ⟨100⟩ face orientation, ⟨100⟩ edge orientation).[26] For sensing ^{1}H nuclei in an external liquid, an electronic-grade diamond sample (EL SC Plate 2.0 × 2.0 × 0.5 mm, ⟨100⟩ face orientation, ⟨110⟩ edge orientation) from Element Six was implanted with ^{14}N.

Palladium films were evaporated onto the different optical-grade samples via an electron beam evaporation system (Temescal BJD 1800). To allow dewetting, the samples were placed in a rapid thermal annealer (RTA) (RX6 from AET Technologies). For the oxygen plasma etching, an inductively coupled plasma (ICP) etcher (Panasonic E640) was used. The chamber pressure of 10 mTorr and an oxygen flow rate of 30 sccm were kept constant for all the experiments, while the RF and ICP powers were varied. The scanning electron microscopy (SEM) images were obtained using a JEOL 7600F and a Hitachi S-5200 at different angles.

The characterization of the nanostructured sample with incorporated NVs was carried out using a homebuilt confocal microscope that allows for diffraction-limited localization of individual color centers and full control of associated electron and nuclear spins.

RESULTS AND DISCUSSION

To determine suitable parameters for dewetting, the palladium thickness and the dewetting temperature were studied. Three optical-grade samples were prepared with thin palladium films. Each sample was divided into three areas with palladium film thicknesses of 3, 6, and 9 nm (Figure 2C). Thereafter, the three samples were annealed for 6 min under nitrogen at either 500, 600, or 700 °C. Due to the risk of graphitization, temperatures above 700 °C were avoided and therefore not studied.[27]

The results of varying the film thickness and the temperature are shown in Figure 2A. Three main effects can be determined from this figure: first, with increasing temperature, the metal features become more separated, convex, and smaller. Second, thinner films are easier to dewet, that is, the thinner the films are, the higher the chance of receiving well-separated circular metal features. Third, the thicker the initial palladium film, the larger the final metal feature diameter. The average diameters given in the figure were calculated via ImageJ.[28] All three observations are in accordance with the theory of the melting-point depression.[23]

The tunability of the feature size is beneficial for sensing and hyperpolarization applications. As an example, for hyperpolarization applications, we maximize the polarization of the external nuclei by reducing pitch. Reducing pitch means reducing spin diffusion length, which minimizes polarization loss due to longitudinal spin relaxation (T_1). The feature size is therefore tuned based on a characteristic spin diffusion length of the target nucleus of choice.

We target a feature size of 100 nm with a 200 nm pitch to avoid spin diffusion lengths above 50 nm, maintaining a minimum detectable volume for an NMR sensor in between

https://doi.org/10.1021/acsomega.2c04250
ACS Omega 2022, 7, 31544−31550

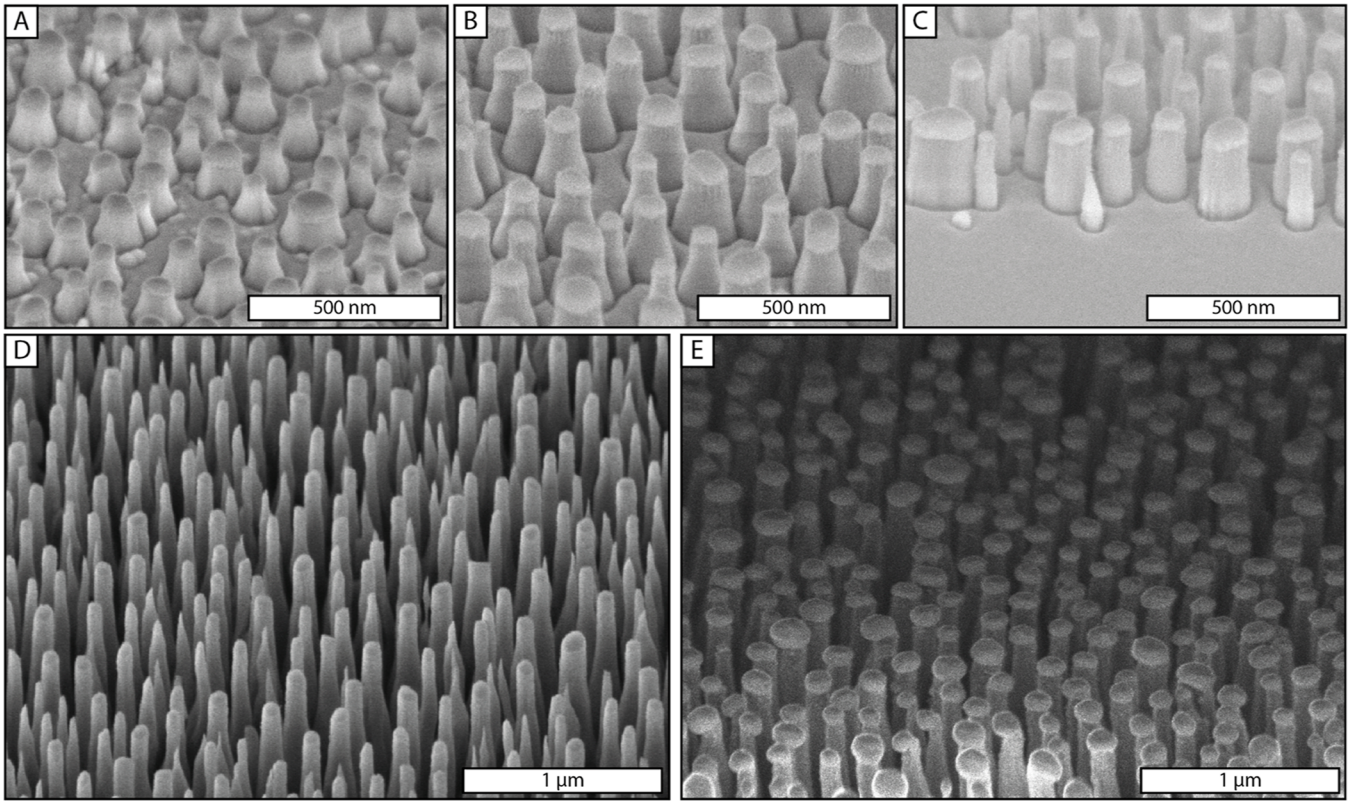

Figure 3. Comparison of different feature geometries. (A–C) show the geometry depending on the RF powers used during the dry etch. The samples were etched for 1 min and the RF powers vary from (A) 50, (B) 100, to (C) 200 W. Further parameters: ICP power: 800 W, pressure: 10 mTorr, O_2 flow rate: 30 sccm (SEM parameters: 2 kV acceleration voltage, 10 μA current, 30° tilt angle). (D) Nanopillars after 4 min of etching and subsequent aqua regia clean (SEM parameters: 2 kV acceleration voltage, 10 μA current, 45° tilt angle). (e) Nanopillars after mask renewal and subsequent dewetting (SEM parameters: 2 kV acceleration voltage, 10 μA current, 30° tilt angle).

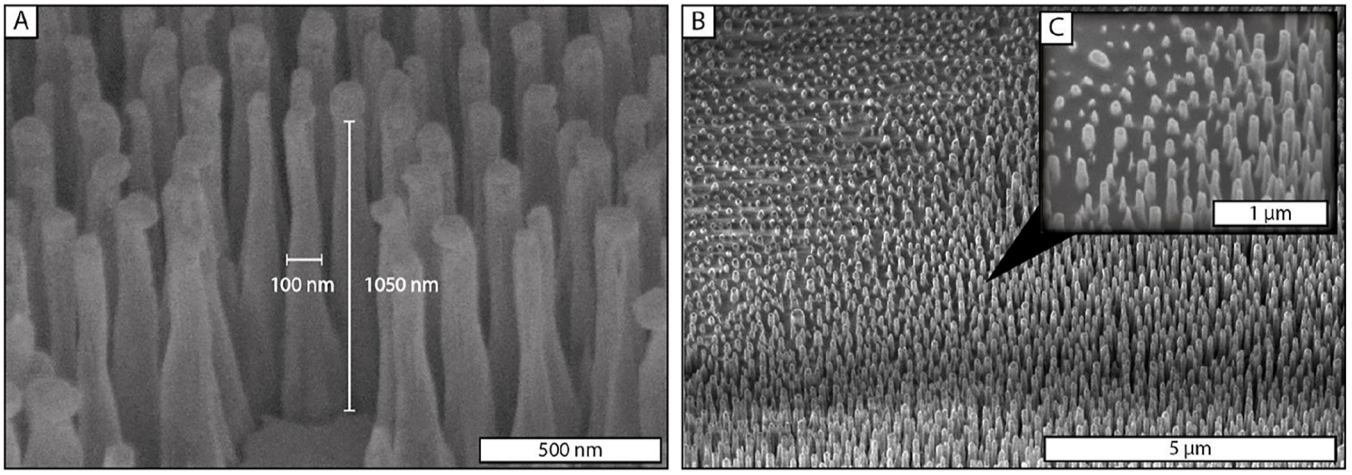

Figure 4. (A) Void in the nanostructure gives insight into the full shape of the nanopillars after 6 min of etching (SEM parameters: 2 kV acceleration voltage, 10 μA current, 30° tilt angle). (B) Fabricated nanostructure with frozen pyruvic acid wetting the surface. (C) Enlargement of (B), showing that the pyruvic acid is trapped between the pillars (SEM parameters: 2 kV acceleration voltage, 10 μA current, 45° tilt angle).

the pillars. Therefore, we chose to proceed with the 6 nm-film-thickness samples that were thermally treated at 600 °C for 6 min, as shown in Figure 2B. The size and shape of the droplets are uniform throughout the whole 3 × 3 mm^2 area.

To study the effect of the bias RF power in the oxygen dry etch, we prepared three samples according to the process above and varied the RF power in each etching process. Figure 3 shows two main effects from varying RF power: a lower RF power leads to lower etch rates and to a more isotropic etch. We found etch rates of 139 nm/min for an RF power of 50 W, 231 nm/min for an RF power of 100 W, and 254 nm/min for an RF power of 200 W. While the anisotropic physical etch dominates for higher RF power, the isotropic chemical etch dominates for lower RF power. The sidewalls formed in an isotropic etch appear less rough than those created with an anisotropic etch recipe, consistent with previous studies.[10]

https://doi.org/10.1021/acsomega.2c04250
ACS Omega 2022, 7, 31544–31550

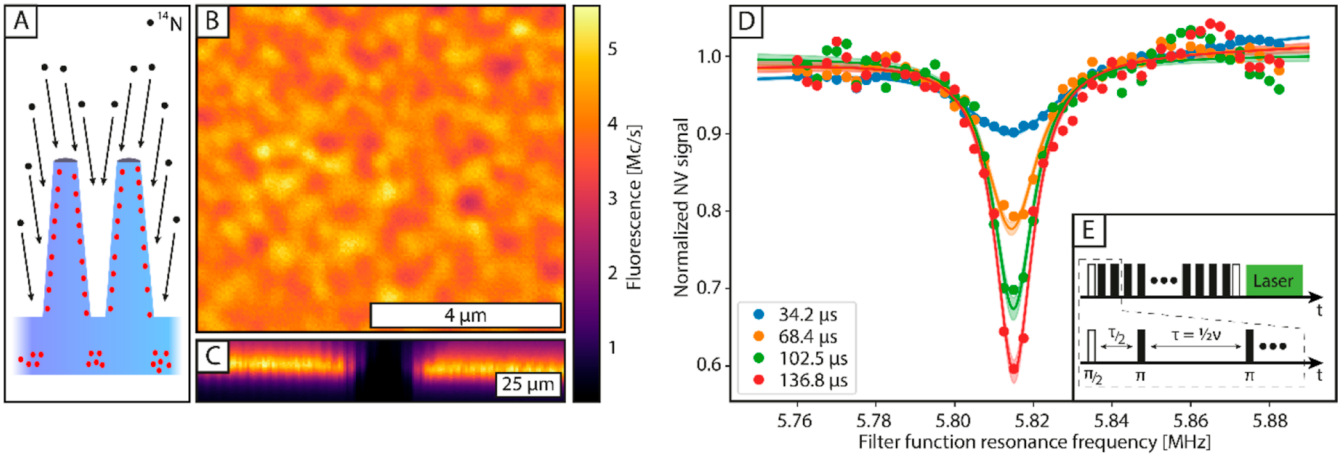

Figure 5. (A) Schematic of the ^{14}N implantation process. Due to the angle at which the nitrogen atoms hit the diamond surface, shallow NVs are created in the pillar sidewalls, and deeper NVs are created below the base of the pillars. Since mask residues on the pillar tops were only removed after the implantation, the nitrogen atoms could not enter the flat horizontal surface on the pillars. (B) Lateral laser scanning confocal fluorescence image of the nanostructured diamond surface with NV centers. For comparison, a single NV center underneath a flat (100) diamond surface and under the same laser excitation and detection conditions would yield a fluorescence photon rate of 1700 counts/s. (C) Depth scan shows the cross section through the diamond surface. The dark region in the center is a shadow cast by the wire, which carries the microwave current for electron spin manipulation. Except for the pillar region of the diamond, no NV fluorescence is visible. (D) NV-based NMR spectroscopy in the region of the ^{1}H Larmor frequency. A spectral line due to statistically polarized ^{1}H spins is visible. For increased coherent interaction time between NV electron spins and ^{1}H spins (values given in legend) the peak amplitude increases, and its linewidth decreases. All NMR spectra are normalized to their respective baseline level. The baseline level itself decreases with interaction time due to decoherence. The average decoherence time of all NV spins in the ensemble is 35(2) μs (see the Supporting Information). NMR measurements were averaged over a 200 μm lateral spot. (E) Illustration of the dynamical decoupling sequence. White and black blocks are $\pi/2$ and π microwave pulses respectively, the green block represents the laser pulse for read out and reinitialization. The π pulse separation τ determines the sensitive frequency ν.

High etch rates and smooth sidewalls are desired for the targeted application of hyperpolarization, and hence, we choose an RF power of 100 W as a good balance for further processes.

The palladium mask eroded almost entirely after 4 min, as shown in Figure 3D. On some of the pillars, which look more pointed than the others, the palladium mask was already gone before the etch process was stopped, and mask erosion transferred to pillar erosion. To renew the mask, we mounted the sample at an angle of 75° in the metal evaporation chamber and evaporated 20 nm from two opposing sides. Thereafter, we treated the sample in the RTA for 6 min at 600 °C. The pillars with the renewed mask are shown in Figure 3E.

The additional palladium mask enabled an extension of the etching time of 2 min. The final features with a height of 1050 nm and a width of 100 nm are shown in Figure 4A. Generally, this process can be iterated as well: we renewed the mask up to three times, which allowed for etching times longer than 10 min and received 1.7 μm tall pillars.

Having formed a nanopillared surface with a large surface area, we next discuss the utility of these structures for quantum-assisted sensing of small volumes of nuclear spins. First, we inferred the wetting of pyruvic acid on the surface of the diamond with cryogenic SEM. A single droplet is placed on the diamond and rapidly frozen in liquid ethane to avoid the condensation of water. A 2 nm layer of platinum as a conductive layer is placed on the sample while keeping it in a cryogenic holder at −196 °C to examine it by SEM. The results are shown in Figure 4B,C. Once a region was found, where the pyruvic acid is present but not overflowing, it was apparent that pyruvic acid is wetting the surface of the nanostructured diamond. Most importantly, the volume between the nanopillars is filled with pyruvic acid, as shown in Figure 4C. Cryogenic SEM revealed no evidence of crystallization, which suggests that pyruvic acid was vitrified. Amorphous glasses are desired as they fill the voids more uniformly than crystals, which is beneficial for hyperpolarization applications.

Finally, we assessed the suitability of our nanostructuring method for NV applications, utilizing a confocal microscope suitable for NV research as, for example, described in ref 29 and the Supporting Information. The confocal microscopy images in Figure 5B,C reveal the implanted NV center ensembles in the nanostructured region of the diamond surface. The interaction between the NV centers and the ^{1}H nuclei in an external liquid (immersion oil) was measured via nanoscale NMR.[9]

To this end, a 200 μm spot of the diamond pillar surface was laser-irradiated and the generated fluorescence was collected (see the Supporting Information for experimental details). A magnetic field of 136.57(4) mT was applied with a misalignment angle of 600(17) μrad with respect to the NV axis. The magnetic field setting was verified by utilizing the optically detected magnetic resonance (ODMR) spectrum of the NV electron spins and the effective hyperfine interaction with the ^{14}N nuclear spins (see the Supporting Information). The measured magnetic field strength yields an expected ^{1}H resonance frequency of 5.816(2) MHz. A dynamical-decoupling-(DD)-based nuclear spin spectroscopy scheme[18] reveals a signal at exactly that frequency, which we identify as the spin noise of the statistically polarized ^{1}H nuclei around each NV center (see Figure 5D and the Supporting Information). The NV ensemble coherence time under the DD sequence is 35(2) μs (see the Supporting Information). The DD sequence is extended to improve the signal acquired from the nuclear spin ensemble, as well as to reduce the spectral linewidth to the limit set by NV centers and ^{1}H spins (see Figure 5D).[30] The NMR signal contrast shown in Figure

https://doi.org/10.1021/acsomega.2c04250
ACS Omega 2022, 7, 31544−31550

5D is of similar strength as for a single center approximately 15 nm deep.[30] The rms field strength of the precessing ^{1}H spins of the oil molecules exert on the NV spins is on the order of 100 nT.[30] The precise distribution of NV center depths and orientations with respect to the diamond surface is not known for the nanostructured diamond presented here. Hence, a precise derivation of average NV depth from NMR signal contrast was not possible.

In addition to these large-volume-averaged NMR spectra, confocal-volume-scale NMR spectra were recorded (see the Supporting Information). They show that the ^{1}H signal mainly originates from the NVs in pillars and not from those at the base of the pillars or from inside the bulk diamond.

CONCLUSIONS

A process for nanostructuring single crystalline diamond using a dewetted palladium film with tunable feature size and pitch as a metal mask for RIE was demonstrated. The aspect ratio of the nanopillars can be increased by renewing the palladium mask to allow for longer etching times. Using this procedure, diamond samples specifically tailored for hyperpolarization and sensing applications with NV centers could be produced in a high-throughput fashion and studied. Via cryogenic SEM, we verified that pyruvic acid, an interesting molecule for metabolic imaging, wets the nanostructured surface. Furthermore, the sample was implanted with ^{14}N and annealed to create NV centers. With a confocal microscope, the NV centers in the nanostructured diamond were utilized for sensing ^{1}H magnetization external to the diamond. The results show that the NV centers are close enough to the diamond surface with a sufficiently high coherence time (35(2) μs) to sense ^{1}H nuclei in the immersion oil. Finally, this procedure enables the possibility to fabricate hundreds of diamond samples in a single day with a single metal evaporator and RIE, whereas fabrication via EBL would need approximately 1 day to produce one similarly nanostructured 3 × 3 mm^2 sample.

ASSOCIATED CONTENT

Supporting Information

The Supporting Information is available free of charge at https://pubs.acs.org/doi/10.1021/acsomega.2c04250.

Diamond surface preparation, implantation of a shallow ensemble of NV centers into the pillar sidewalls, experimental setups for NV-diamond investigations, NV spin measurements with large area averaging, NMR spectroscopy with NV centers in large area ensembles, DD-based spectroscopy, magnetic field alignment and confirmation, and NMR spectroscopy with small NV ensembles with a confocal spatial resolution (PDF)

AUTHOR INFORMATION

Corresponding Author

Martin Gierse − *NVision Imaging Technologies GmbH, 89081 Ulm, Germany; Institute for Quantum Optics, Ulm University, 89081 Ulm, Germany;* orcid.org/0000-0002-8187-5903; Email: martin.gierse@nvision-imaging.com

Authors

Alastair Marshall − *NVision Imaging Technologies GmbH, 89081 Ulm, Germany; Institute for Quantum Optics, Ulm University, 89081 Ulm, Germany*

M. Usman Qureshi − *NVision Imaging Technologies GmbH, 89081 Ulm, Germany*

Jochen Scharpf − *NVision Imaging Technologies GmbH, 89081 Ulm, Germany*

Anna J. Parker − *NVision Imaging Technologies GmbH, 89081 Ulm, Germany*

Birgit J. M. Hausmann − *NVision Imaging Technologies GmbH, 89081 Ulm, Germany*

Paul Walther − *Central Facility for Electron Microscopy, Ulm University, 89081 Ulm, Germany*

Ania C. Bleszynski Jayich − *Department of Physics, University of California Santa Barbara, Santa Barbara, California 93106, United States*

Fedor Jelezko − *NVision Imaging Technologies GmbH, 89081 Ulm, Germany; Institute for Quantum Optics, Ulm University, 89081 Ulm, Germany*

Philipp Neumann − *NVision Imaging Technologies GmbH, 89081 Ulm, Germany*

Ilai Schwartz − *NVision Imaging Technologies GmbH, 89081 Ulm, Germany*

Complete contact information is available at: https://pubs.acs.org/10.1021/acsomega.2c04250

Author Contributions

#M.G. and A.M. contributed equally. The manuscript was written through contributions of all authors. All authors have given approval to the final version of the manuscript.

Notes

The authors declare no competing financial interest.

ACKNOWLEDGMENTS

A.M. would like to acknowledge funding received from the European Union's Horizon 2020 Research and Innovation Programme under the Marie Sklodowska-Curie grant agreement no. 765267 (QuSCo). ABJ acknowledges support from the NSF Quantum Foundry at UCSB through the Q-AMASE-i program under DMR grant 1906325.

ABBREVIATIONS

NV, nitrogen vacancy; NMR, nuclear magnetic resonance; MRI, magnetic resonance imaging; d-DNP, dissolution-dynamic nuclear polarization; rms, root mean square; EBL, electron beam lithography; RIE, reactive ion etching; RTA, rapid thermal annealer; ICP, inductively coupled plasma; SEM, scanning electron microscopy; ODMR, optically detected magnetic resonance; DD, dynamic decoupling

REFERENCES

(1) Gruber, A.; Dräbenstedt, A.; Tietz, C.; Fleury, L.; Wrachtrup, J.; Borczyskowski, C. Scanning Confocal Optical Microscopy and Magnetic Resonance on Single Defect Centers. *Science* **1997**, *276*, 2012.

(2) Ladd, T. D.; Jelezko, F.; Laflamme, R.; Nakamura, Y.; Monroe, C.; O'Brien, J. L. Quantum computers. *Nature* **2010**, *464*, 45.

(3) Beveratos, A.; Brouri, R.; Gacoin, T.; Villing, A.; Poizat, J.-P.; Grangier, P. Single Photon Quantum Cryptography. *Phys. Rev. Lett.* **2002**, *89*, 18.

(4) Awschalom, D. D.; Epstein, R.; Hanson, R. THE DIAMOND AGE OF SPINTRONICS. *Sci. Am.* **2007**, *297*, 84.

(5) Balasubramanian, G.; Chan, I. Y.; Kolesov, R.; Al-Hmoud, M.; Tisler, J.; Shin, C.; Kim, C.; Wojcik, A.; Hemmer, P. R.; Krueger, A.; Hanke, T.; Leitenstorfer, A.; Bratschitsch, R.; Jelezko, F.; Wrachtrup,

J. Nanoscale imaging magnetometry with diamond spins under ambient conditions. *Nature* **2008**, *455*, 648.
(6) Mamin, H. J.; Kim, M.; Sherwood, M. H.; Rettner, C. T.; Ohno, K.; Awschalom, D. D.; Rugar, D. Nanoscale Nuclear Magnetic Resonance with a Nitrogen-Vacancy Spin Sensor. *Science* **2013**, *339*, 557.
(7) Breeze, J. D.; Salvadori, E.; Sathian, J.; Alford, N. M.; Kay, C. W. M. Continuous-wave room-temperature diamond maser. *Nature* **2018**, *555*, 493.
(8) Broadway, D. A.; Tetienne, J.-P.; Stacey, A.; Wood, J. D. A.; Simpson, D. A.; Hall, L. T.; Hollenberg, L. C. L. Quantum probe hyperpolarisation of molecular nuclear spins. *Nat. Commun.* **2018**, *9*, 1246.
(9) Kehayias, P.; Jarmola, A.; Mosavian, N.; Fescenko, I.; Benito, F. M.; Laraoui, A.; Smits, J.; Bougas, L.; Budker, D.; Neumann, A.; Brueck, S. R. J.; Acosta, V. M. Solution nuclear magnetic resonance spectroscopy on a nanostructured diamond chip. *Nat. Commun.* **2017**, *8*, 188.
(10) Hausmann, B. J. M.; Khan, M.; Zhang, Y.; Babinec, T. M.; Martinick, K.; McCutcheon, M.; Hemmer, P. R.; Lončar, M. Fabrication of diamond nanowires for quantum information processing applications. *Diamond Relat. Mater.* **2010**, *19*, 621.
(11) Sørensen, O. W.; Keeler, J. Understanding NMR Spectroscopy; John Wiley & Sons, 2006; Vol. *44*(8), p 8.
(12) Waldherr, G.; Beck, J.; Steiner, M.; Neumann, P.; Gali, A.; Frauenheim, Th.; Jelezko, F.; Wrachtrup, J. Wrachtrup, "Dark States of Single Nitrogen-Vacancy Centers in Diamond Unraveled by Single Shot NMR. *Phys. Rev. Lett.* **2011**, *106*, 15.
(13) Abrams, D.; Trusheim, M. E.; Englund, D. R.; Shattuck, M. D.; Meriles, C. A. Dynamic Nuclear Spin Polarization of Liquids and Gases in Contact with Nanostructured Diamond. ACS Publications, Apr. 28, 2014. https://pubs.acs.org/doi/pdf/10.1021/nl500147b (accessed Jan 19, 2022).
(14) Kurhanewicz, J.; Vigneron, D. B.; Brindle, K.; Chekmenev, E. Y.; Comment, A.; Cunningham, C. H.; DeBerardinis, R. J.; Green, G. G.; Leach, M. O.; Rajan, S. S.; Rizi, R. R.; Ross, B. D.; Warren, W. S.; Malloy, C. R. Analysis of Cancer Metabolism by Imaging Hyperpolarized Nuclei: Prospects for Translation to Clinical Research. *Neoplasia* **2011**, *13*, 81.
(15) Sangtawesin, S.; Dwyer, B. L.; Srinivasan, S.; Allred, J. J.; Rodgers, L. V. H.; De Greve, K.; Stacey, A.; Dontschuk, N.; O'Donnell, K. M.; Hu, D.; Evans, D. A.; Jaye, C.; Fischer, D. A.; Markham, M. L.; Twitchen, D. J.; Park, H.; Lukin, M. D.; de Leon, N. P. Origins of Diamond Surface Noise Probed by Correlating Single-Spin Measurements with Surface Spectroscopy. *Phys. Rev. X* **2019**, *9*, 031052.
(16) Albers, M. J.; Bok, R.; Chen, A. P.; Cunningham, C. H.; Zierhut, M. L.; Zhang, V. Y.; Kohler, S. J.; Tropp, J.; Hurd, R. E.; Yen, Y. F.; Nelson, S. J.; Vigneron, D. B.; Kurhanewicz, J. Hyperpolarized 13C Lactate, Pyruvate, and Alanine: Noninvasive Biomarkers for Prostate Cancer Detection and Grading. *Cancer Res.* **2008**, *68*, 8607.
(17) Lafon, O.; Thankamony, A. S. L.; Kobayashi, T.; Carnevale, D.; Vitzthum, V.; Slowing, I. I.; Kandel, K.; Vezin, H.; Amoureux, J.-P.; Bodenhausen, G.; Pruski, M. Mesoporous Silica Nanoparticles Loaded with Surfactant: Low Temperature Magic Angle Spinning 13 C and 29 Si NMR Enhanced by Dynamic Nuclear Polarization. *J. Phys. Chem. C* **2013**, *117*, 1375−1382.
(18) Staudacher, T.; Shi, F.; Pezzagna, S.; Meijer, J.; Du, J.; Meriles, C. A.; Reinhard, F.; Wrachtrup, J. Nuclear Magnetic Resonance Spectroscopy on a (5-Nanometer) 3 Sample Volume. *Science* **2013**, *339*, 561−563.
(19) Huang, T.-Y.; Grote, R. R.; Mann, S. A.; Hopper, D. A.; Exarhos, A. L.; Lopez, G. G.; Klein, A. R.; Garnett, E. C.; Bassett, L. C. A monolithic immersion metalens for imaging solid-state quantum emitters. *Nat. Commun.* **2019**, *10*, 2392.
(20) Hausmann, B. J. M.; Shields, B. J.; Quan, Q.; Chu, Y.; de Leon, N. P.; Evans, R.; Burek, M. J.; Zibrov, A. S.; Markham, M.; Twitchen, D. J.; Park, H.; Lukin, M. D.; Loncăr, M. Coupling of NV Centers to Photonic Crystal Nanobeams in Diamond. *Nano Lett.* **2013**, *13*, 5791.
(21) Trusheim, M. E.; Li, L.; Laraoui, A.; Chen, E. H.; Bakhru, H.; Schröder, T.; Gaathon, O.; Meriles, C. A.; Englund, D. Scalable Fabrication of High Purity Diamond Nanocrystals with Long-Spin-Coherence Nitrogen Vacancy Centers. *Nano Lett.* **2014**, *14*, 32−36.
(22) Janssen, W.; Gheeraert, E. Dry etching of diamond nanowires using self-organized metal droplet masks. *Diamond Relat. Mater.* **2011**, *20*, 389.
(23) Pawlow, P. Über den Einfluß der Oberfläche einer festen Phase auf die latente Wärme und die Temperatur des Schmelzens. *Z. Chem. Ind. Kolloide* **1910**, *7*, 37.
(24) Takagi, M. Electron-Diffraction Study of Liquid-Solid Transition of Thin Metal Films. *J. Phys. Soc. Jpn.* **1954**, *9*, 359.
(25) Gao, F.; Nebel, C. E. Diamond nanowire forest decorated with nickel hydroxide as a pseudocapacitive material for fast charging−discharging. *Phys. Status Solidi A* **2015**, *212*, 2533.
(26) https://www.e6.com. [Online]. Available: https://www.e6.com/en (accessed 2022-06-01).
(27) Fedoseev, D. V.; Vnukov, S. P.; Bukhovets, V. L.; Anikin, B. A. Surface graphitization of diamond at high temperatures. *Surf. Coat. Technol.* **1986**, *28*, 207.
(28) Schneider, C. A.; Rasband, W. S.; Eliceiri, K. W. NIH Image to ImageJ: 25 years of image analysis. *Nat. Methods* **2012**, *9*, 671.
(29) Pfender, M.; Aslam, N.; Waldherr, G.; Neumann, P.; Wrachtrup, J. Single-spin stochastic optical reconstruction microscopy. *Proc. Natl. Acad. Sci. U.S.A.* **2014**, *111*, 14669−14674.
(30) Pham, L. M.; DeVience, S. J.; Casola, F.; Lovchinsky, I.; Sushkov, A. O.; Bersin, E.; Lee, J.; Urbach, E.; Cappellaro, P.; Park, H.; Yacoby, A.; Lukin, M.; Walsworth, R. L. NMR technique for determining the depth of shallow nitrogen-vacancy centers in diamond. *Phys. Rev. B* **2016**, *93*, 045425.

https://doi.org/10.1021/acsomega.2c04250
ACS Omega 2022, 7, 31544−31550